Nanoscale

PAPER

View Article Online
View Journal | View Issue

Check for updates

Cite this: *Nanoscale*, 2018, **10**, 15078

Regioselectivity of the Pauson–Khand reaction in single-walled carbon nanotubes†

Juan Pablo Martínez, *[a] María Vizuete, [b] Luis M. Arellano, [b] Albert Poater, [a] F. Matthias Bickelhaupt, [c,d] Fernando Langa *[b] and Miquel Solà *[a]

Received 28th April 2018,
Accepted 20th July 2018

DOI: 10.1039/c8nr03480j

rsc.li/nanoscale

Chemical functionalization of nanotubes, in which their properties can be combined with those of other classes of materials, is fundamental to improve the physicochemical properties of nanotubes for potential technological applications. In this work, we theoretically and experimentally examine the Pauson–Khand reaction (PKR) on zig-zag, armchair, and chiral single-walled carbon nanotubes (SWCNTs). Our benchmarked density functional theory (DFT) calculations show that an alternative pathway to the widely accepted Magnus reaction pathway has significantly lower energy barriers, thus suggesting the use of this alternative pathway to predict whether a PKR on SWCNTs is favored or hampered. Accessible energy barriers of up to 16 kcal mol^{-1} are estimated and our results suggest that semiconducting SWCNTs react faster than metallic ones, although both types can be functionalized. Guided by our theoretical predictions, cyclopentenones are successfully attached to SWCNTs by heating and are, subsequently, characterized in the laboratory.

Open Access Article. Published on 25 July 2018. Downloaded on 2/11/2026 3:22:22 AM.
This article is licensed under a Creative Commons Attribution 3.0 Unported Licence.

Introduction

First reported in the early 1970s by Pauson and Khand *et al.*, the [2 + 2 + 1] cycloaddition between an alkene, an alkyne, and a carbon monoxide unit (CO) leads to the formation of cyclopentenones mediated or catalyzed by a transition metal; originally a complex of cobalt(0) (see Scheme 1).[1–3] This chemical transformation, usually termed as the Pauson–Khand reaction (PKR), has gained attention within the field of organic chemistry since many natural products can be synthesized from it.[4–18] Besides cobalt, also other transition metals perform well in the PKR such as rhodium,[19–21] ruthenium,[22,23] palladium,[24] iridium,[25,26] iron,[27,28] tungsten,[29] molybdenum,[30,31] and chromium.[32,33]

The PKR depends upon steric and electronic factors. From Scheme 1, one would expect up to sixteen different isomers; two regioisomers due to the groups X_1 and X_2 in the alkene, two regioisomers because of the groups X_3 and X_4 in the alkyne, and four enantiomers originating from each one of the four mentioned regioisomers. However, the alkene stereochemistry remains intact according to the reaction mechanism and only two stereoisomers are possible. That is, in the case of *cis*-alkenes the groups in stereocenters X_1 and X_2 always end up on the same side of the ring. In this regard, the theoretical products of a PKR may be predicted based on steric arguments, but selectivity also depends on electronic factors. That is, the carbon atom of the alkyne substituted by an electron-donating or a larger group usually ends up at the α-position in the resulting cyclopentenone, leaving the β-position to the alkyne carbon atom substituted by an electron-withdrawing or a smaller group as depicted in Scheme 1. These observations

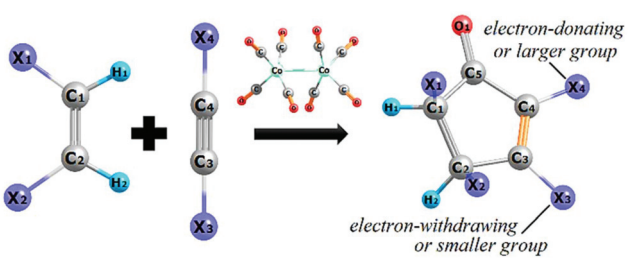

Scheme 1 The Pauson–Khand reaction and its regiochemistry.

[a]*Institut de Química Computacional i Catàlisi and Departament de Química, Universitat de Girona, Campus Montilivi, 17003-Girona, Spain. E-mail: tema_juanpablo@hotmail.com, miquel.sola@udg.edu*
[b]*Universidad de Castilla-La Mancha, Instituto de Nanociencia, Nanotecnología y Materiales Moleculares (INAMOL), 45071-Toledo, Spain. E-mail: fernando.Langa@uclm.es*
[c]*Department of Theoretical Chemistry and Amsterdam Center for Multiscale Modeling (ACMM), Vrije Universiteit Amsterdam, De Boeleaan 1083, NL-1081 HV Amsterdam, The Netherlands*
[d]*Institute of Molecules and Materials (IMM), Radboud University, Heyendaalseweg 135, NL-6525 AJ Nijmegen, The Netherlands*

†Electronic supplementary information (ESI) available: Experimental evidence, detailed discussion of reaction mechanisms that are not included in the main manuscript, benchmarking methodology, structural analysis of some optimized geometries, and energies and cartesian coordinates of all located stationary points. See DOI: 10.1039/c8nr03480j

This journal is © The Royal Society of Chemistry 2018

Open Access Article. Published on 25 July 2018. Downloaded on 2/11/2026 3:22:22 AM.
This article is licensed under a Creative Commons Attribution 3.0 Unported Licence.

were confirmed by analyzing a series of alkynes with substituents electronically and/or sterically differentiated.[34,35] In fact, based on a study regarding diarylalkynes, it can be demonstrated that the alkyne polarization *via* inductive effect has a significant impact on the regioselectivity of the PKR.[36,37]

The scope of the PKR and variations thereof encompasses several functional groups.[38] Two approaches can be distinguished: intramolecular and intermolecular PKR. In the case of the intramolecular version, some of us previously demonstrated that fulleropyrrolidines endowed with one or two propargyl groups at the C-2 position of the pyrrolidine ring (1,6-enynes) undergo the PKR leading to cyclopentenones fused to the fullerene moiety.[39,40] On the other hand, there are studies in which cyclopentenones are successfully synthesized *via* intermolecular PKR;[41–44] although this approach is more limited since olefins without strain are poorly reactive with the exception of ethylene.[45,46] Studies on the chemical functionalization of carbon nanostructures *via* the PKR are rather scarce and, to our knowledge, this cycloaddition has not been studied in single-walled carbon nanotubes (SWCNTs) yet. These materials have attracted interest due to their remarkable physical properties.[47–53] Besides, functionalized SWCNTs have become useful assemblies in the fields of materials, medical, and biological sciences.[54–56] Nonetheless, the actual application of these materials may be hindered because their selective purification is hard to achieve due to their poor solubility in conventional solvents or the formation of agglomerates because of strong π-stacking tendencies.[57,58] These problems can be partially or totally solved with proper chemical modifications.[59–62] In view of that, in this contribution the PKR in SWCNTs is first quantum-chemically explored with the aim of analyzing whether the PKR can be a suitable synthetic strategy for the chemical functionalization of SWCNTs. Then, the PKR is experimentally proved and added to the toolbox of chemical reactions useful to functionalize SWCNTs.

The generally accepted reaction mechanism was initially proposed by Magnus *et al.*;[63,64] subsequently, theoretical studies by Nakamura[65] and Pericàs[66] *et al.* based on density functional theory (DFT) corroborated the main steps of the reaction. Within the purposes of the current manuscript, a graphical representation of the overall PKR mechanism in SWCNTs with 2-heptyne as the alkyne and catalyzed by dicobalt octacarbonyl [$Co_2(CO)_8$] is provided in Scheme 2.

Results and discussion

This section is outlined as follows. Computational investigations are firstly introduced starting with the description of the models used in the quantum-chemical modeling of reactions in SWCNTs. The main goal in this subsection is to validate the approach implemented in the current study. After that, the complexation step is discussed in detail to introduce an alternative pathway to the generally-accepted mechanism. The PKR in armchair, zig-zag, and chiral SWCNTs with 2-heptyne is described in the following subsections (the PKR

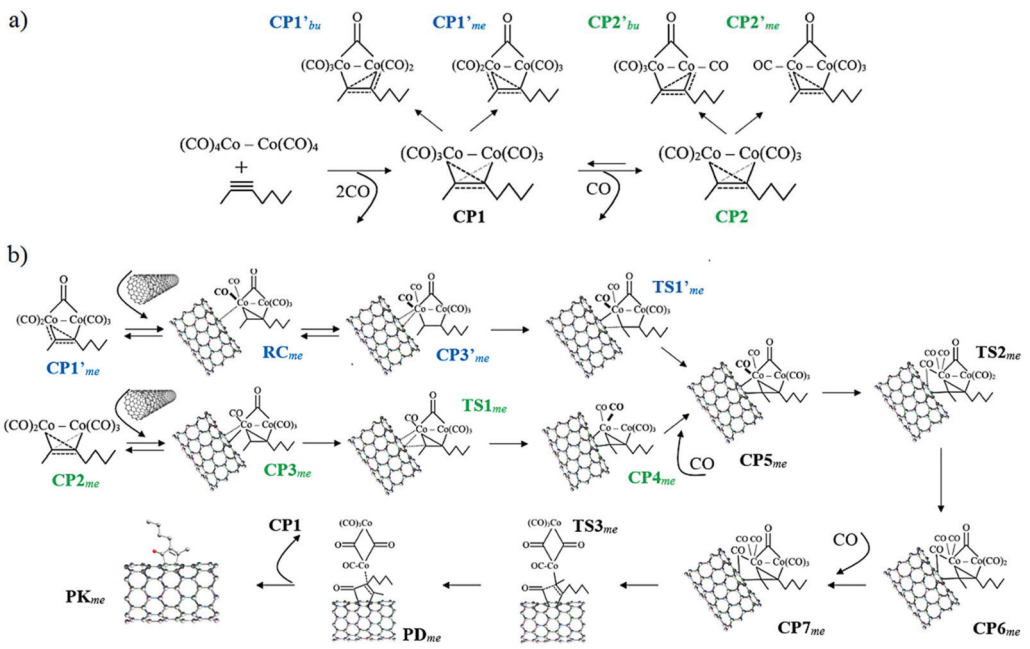

Scheme 2 Mechanism of the Pauson–Khand reaction in single-walled carbon nanotubes with 2-heptyne as the alkyne and dicobalt octacarbonyl [$Co_2(CO)_8$] as the catalyst. (a) Complexation between $Co_2(CO)_8$ and 2-heptyne. (b) Progress of the reaction from the nanotube insertion. Blue and green labels respectively correspond to the alternative and generally-accepted pathways. The alternative pathway converges to the generally-accepted mechanism from **CP5** (black labels). Labels given as in a previous work[65] along with subscripts indicating what carbon atom of the alkyne react first: the one linked to methyl "*me*" or butyl "*bu*".

Open Access Article. Published on 25 July 2018. Downloaded on 2/11/2026 3:22:22 AM.
This article is licensed under a Creative Commons Attribution 3.0 Unported Licence.

with acetylene is illustrated in Fig. S1,† see also related discussion). Then, the main factors inducing the regioselectivity of the PKR are analyzed in terms of structural conformations and electronic interactions. Finally, experimental investigations demonstrating the successful synthesis of cyclopentenones attached to SWCNTs provide evidences that strengthen the conclusions achieved from the quantum-chemical study.

All mechanisms are formulated under the following description (see Scheme 2). In the initial step, that is complexation, $Co_2(CO)_8$ releases two CO and coordinates with the alkyne substrate. The resulting complex of cobalt, **CP1**, reversibly releases a third CO thus forming **CP2**. Then the wall of a SWCNT reaches the coordination sphere of a cobalt atom with a vacant site in **CP2** and forms **CP3**. Upon the reversible SWCNT coordination, the SWCNT insertion takes place resulting in the formation of a cobaltacycle, **CP4**. Then, this intermediate recovers one CO giving rise to **CP5**. The resulting cobaltacycle in **CP5** can be formed *via* an alternative pathway, in which both first coordination spheres of the two cobalt atoms keep six CO units instead of five through every step (see pathway starting from **CP1′** in Scheme 2b). This step is important because the course of the PKR is usually determined by the nanotube insertion since the regiochemistry and stereochemistry of the final adduct can be controlled from this step. The CO insertion generates the next intermediate, **CP6**, and a subsequent coordination of another CO to cobalt gives rise to **CP7**. A reductive elimination leads to the pre-product, **PD**, and the decomplexation step produces the final adduct, **PK**. The theoretical work is therefore based on this description for the PKR in SWCNTs with acetylene or 2-heptyne as the alkyne. 2-Heptyne is included in this study because it reduces experimental difficulties associated to the manipulation of acetylene; besides, results based on an asymmetric alkyne strengthen the conclusions derived in this work.

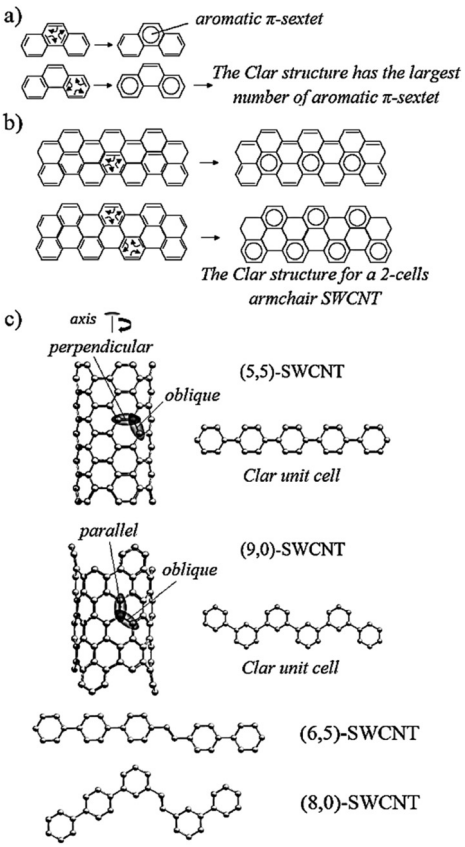

Scheme 3 Graphical representation of Clar's aromatic π-sextet rule in (a) phenanthrene, and (b) a 2-cell SWCNT. The rule states that a Clar structure is the one with the largest number of aromatic π-sextets, and it better agrees with experimental evidence. (c) The SWCNT structures studied in this work. The picture also illustrates the cycloadditions to the parallel, oblique, and perpendicular positions relative to the nanotube axis.

Computational investigations

Modeling chemical reactions in SWCNTs. Before formulating the reaction mechanisms of interest, it is convenient to describe the models used to reach the purposes of this work. Quantum-chemical modeling of chemical reactions in SWCNTs can be appropriately done with chemical structures regarding the Clar theory (see Scheme 3a and b).[67–72] Clar networks are more stable than their counterpart Kekulé structures as aromaticity provides some extra stability to conjugated systems.[73–77] Following this order of ideas, the PKR is studied by taking into consideration an armchair SWCNT with chiral indices (5,5) (6.78 Å of diameter) and a zig-zag SWCNT with chiral indices (9,0) (7.05 Å of diameter). The length of both structures is 3-Clar unit cells [*ca.* 12.20 Å for (5,5)-SWCNT and 11.20 Å for (9,0)-SWCNT]. Some advantages can be achieved by using Clar networks since these are fully benzenoid structures, have a closed-shell singlet ground state with frontier molecular orbitals entirely delocalized, and faster convergence can be reached in their electronic properties with respect to the number of unit cells. All these features are not true for conventional models of SWCNTs. For instance, the ground state of a non-Clar (9,0)-SWCNT is a quintet spin state with the four frontier electrons completely localized at the edges of the nanotube.[67,78] The Clar structures considered in this manuscript and the available reaction sites for the PKR are depicted in Scheme 3c, as well as the Clar unit cells for (6,5)- and (8,0)-SWCNT. Additionally, metallic SWCNTs are defined with the (n,n) chiral indices, semimetallic with (n,0) (n a multiple of 3), and otherwise they are semiconductors.

The complexation step. Among all the chemical species shown in Scheme 2a, only **CP1** has been completely isolated and characterized.[79] Some photochemical studies reveal the successful trapping of intermediates like **CP2**, in which cobalt is not only coordinated to an alkyne but also to other species.[80–83] We are not aware of any study regarding the trapping of an isolated **CP2**. Moreover, McGlinchey *et al.* demonstrated that elimination of CO to form **CP2** can be difficult for some ethynyl complexes; in addition, they concluded that some pentacarbonyl complexes, **CP2**, do not continue along the Magnus pathway because of the unfavorable relative orientation of the cobalt-coordinated alkyne and alkene.[84]

 This journal is © The Royal Society of Chemistry 2018

Open Access Article. Published on 25 July 2018. Downloaded on 2/11/2026 3:22:22 AM.
This article is licensed under a Creative Commons Attribution 3.0 Unported Licence.

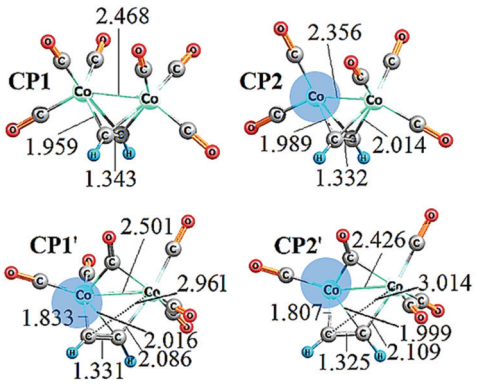

Fig. 1 Main bond distances (in Å) for the structures involved in the complexation step. A shaded region represents a vacant site on a cobalt atom.

Some bond distances for the **CP1** (**CP1′**) and **CP2** (**CP2′**) structures formed with acetylene are shown in Fig. 1. In all the cases, the C–C bond shows a double-bond character (typical ethylene C–C bond distance, *ca.* 1.33 Å). The Co–Co distance enlarges when the number of coordinated CO ligands increases going from 2.36 Å in **CP2** to 2.47 Å in **CP1** and from 2.43 Å in **CP2′** to 2.50 Å in **CP1′**. The four C(alkyne)–Co bond distances remain more or less constant in **CP1** and **CP2**, 1.96 and 2.01 Å, respectively.

The **CP1′** and **CP2′** structures differ from **CP1** and **CP2** in the coordination of one CO unit as it is μ_2-coordinated to both Co atoms. As a matter of fact, CO-bridging ligand complexes have been previously reported.[85] Moreover, the distances of 1.83 and 2.96 Å in **CP1′** between C–Co suggest that only one Co atom is η^2-coordinated to the alkyne, and the other is η^1-coordinated. A similar observation is done for **CP2′**. As a concluding remark, a vacant site in cobalt, wherein the coordination with an olefin can occur, like the one in **CP2** can be also formed without releasing another CO from **CP1** due to a simple geometrical rearrangement leading to **CP1′** (see Fig. 1).

The analysis outlined in this subsection has direct consequences in the energetics and, in turn, the formulation of the reaction mechanism for the PKR. The relative thermodynamic stability of the **CP1** (**CP1′**) and **CP2** (**CP2′**) structures is reported in Table 1. The **CP1′** structure seems to describe better the complexation step based on thermodynamic arguments, which is attributed to the fact that the decoordination of another CO from **CP1** to form **CP2** (**CP2′**) leads to a Co atom that disobeys the 18-electron rule, which is not common for the first-row transition metals like cobalt, thus causing a strong thermodynamic destabilization of the species.

In the case of the structures formed with 2-heptyne, there are two regioisomers of **CP1′** and **CP2′** which depend on the group that is linked to the cobalt atom with the vacant site. For instance, $\mathbf{CP1'}_{me}$ means that the alkyne carbon atom with the methyl group is linked to the metal with the vacant site, then this carbon atom undergoes first the alkene or SWCNT insertion. As illustrated in Table 1, the thermodynamic stability follows the sequence $\mathbf{CP2'}_{bu}$ < $\mathbf{CP2'}_{me}$ < **CP2** < $\mathbf{CP1'}_{bu}$ < $\mathbf{CP1'}_{me}$ < **CP1**, and once again the $\mathbf{CP1'}_{me}$ and $\mathbf{CP1'}_{bu}$ structures are more suitable to describe the complexation step.

Nakamura's DFT-results in the case of the electronic energy of **CP2** with acetylene strongly differ from ours. They calculated an electronic energy of **CP2** relative to **CP1** of 26.4 and 21.2 kcal mol^{-1} at the B3LYP[86,87]/631LAN and B3LYP/6311SDD//B3LYP/631LAN levels of theory, respectively.[65] In this regard, Table 1 shows that **CP2** is highly destabilized since its electronic energy is 57 kcal mol^{-1} higher than that of **CP1**. It is not easy to identify the reason of such a large difference. It could be related to the use of a different hybrid functional along with gaussian basis sets in Nakamura's calculations. Nevertheless, it is likely that the main difference comes from the methodology used by Nakamura and coworkers that does not include relativistic corrections *via* the zeroth-order regular approximation, the frozen-core approximation, solvent effects associated to a large dielectric constant (33.0), and dispersion corrections (see below Computational details). However, as far as we know, there are no studies regarding structures like **CP1′**, which certainly is more stable than **CP2**. Even if we are overestimating the energy of both complexes, **CP1′** in fact keeps six CO units so that the 18-electron rule is fulfilled in the cobalt atom with the vacant site thus gaining stability, unlike the cobalt atom in **CP2** with the vacant site generated by the removal of CO from **CP1**.

The PKR in metallic SWCNTs. A detailed discussion concerning the complexation step was given in the previous subsection with the aim of introducing an alternative reaction pathway to the generally-accepted Magnus mechanism.[63,64] In this subsection, both mechanisms are compared for the PKR in metallic (5,5)-SWCNTs. Changes in Gibbs energy are given with respect to the energy of **CP1** since the formation of this complex is common for any PKR, although it is formed in a preactivation step from $Co_2(CO)_8$ and acetylene or 2-heptyne with an energy cost of ΔG ~18 kcal mol^{-1}.

The nomenclature defined in Schemes 2 and 3c is jointly adopted in this subsection; that is, if the alkyne carbon atom with the methyl group is initially linked to the oblique position of the nanotube, then a **PK** adduct can be generated in what we called the "methyl" pathway, $\mathbf{PK}_{me,obl}$ (Fig. 2a). The distinction in the reaction pathways is given by the nanotube insertion. Because of symmetry arguments, only one **PK** adduct at the perpendicular position is possible, $\mathbf{PK}_{me,per}$. Nonetheless,

Table 1 Comparison of relative electronic and Gibbs energies (in kcal mol^{-1}) for structures formed in the complexation step

Acetylene			2-Heptyne		
Species	ΔE_{rel}	ΔG_{rel}	Species	ΔE_{rel}	ΔG_{rel}
CP1	0.0	0.0	**CP1**	0.0	0.0
CP1′	16.5	16.7	$\mathbf{CP1'}_{me}$	17.5	15.8
CP2	56.9	43.9	$\mathbf{CP1'}_{bu}$	18.7	16.0
CP2′	70.7	58.2	**CP2**	56.3	40.6
			$\mathbf{CP2'}_{me}$	72.6	58.4
			$\mathbf{CP2'}_{bu}$	73.8	59.4

Open Access Article. Published on 25 July 2018. Downloaded on 2/11/2026 3:22:22 AM.
This article is licensed under a Creative Commons Attribution 3.0 Unported Licence.

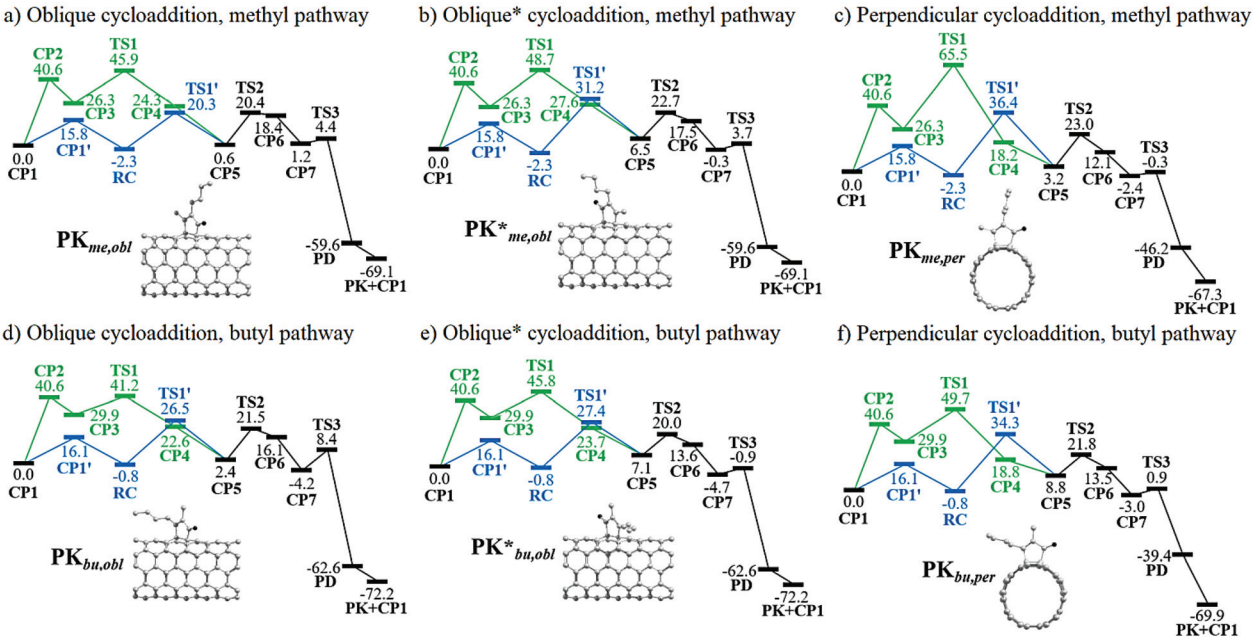

Fig. 2 Gibbs energy profiles in kcal mol^{-1} for the Pauson–Khand reaction with 2-heptyne in (5,5)-SWCNT. Blue and green lines respectively correspond to the alternative and generally-accepted pathways. The alternative pathway converges to the generally-accepted mechanism (black lines).

it can be observed in Scheme 3c that the formation of **PK** at the oblique position can be done *via* two pathways. Given the insertion of one carbon of the alkyne to one carbon localized at the perpendicular position of the nanotube, the cycloaddition leading to **PK** can evolve to either the perpendicular or oblique position; labeled the latter as **PK**$_{me,obl}$. Otherwise, the produced adduct is **PK***$_{me,obl}$. Therefore, six **PK** adducts can be differentiated: **PK**$_{me,obl}$, **PK***$_{me,obl}$, **PK**$_{me,per}$, **PK**$_{bu,obl}$, **PK***$_{bu,obl}$, and **PK**$_{bu,per}$; wherein the three later adducts are originated when the alkyne carbon atom with the butyl group is linked to the nanotube, *i.e. via* the "butyl" pathway.

A graphical representation of the different pathways related to the PKR in (5,5)-SWCNT with 2-heptyne is given in Fig. 2. The nanotube coordination in the Magnus mechanism is an endergonic process forming **CP3** from **CP1** by more than 26 kcal mol^{-1} with an energy barrier of 40.6 kcal mol^{-1}. On the other hand, this step is slightly exergonic with an energy barrier of *ca.* 16 kcal mol^{-1} in the alternative pathway that leads to a reactant complex **RC**. Then, within the Magnus mechanism, the nanotube insertion is an exergonic process to form **CP4** from **CP3** which releases from 2 to 11 kcal mol^{-1}, except for the slightly endergonic process *via* a methyl oblique cycloaddition (forming **CP4***$_{me,obl}$). The energy barriers in these cases range from 11 to 39 kcal mol^{-1}, being the lowest and highest ones *via* **TS1**$_{bu,obl}$ and **TS1**$_{me,per}$, respectively. These results suggest that the nanotube insertion through the Magnus mechanism should occur at the oblique position and *via* the butyl pathway. In contrast, the nanotube insertion *via* the alternative pathway is an endergonic process requiring an energy from 3 to 10 kcal mol^{-1} to form **CP5** from **RC**. This step has an energy barrier from 23 to 39 kcal mol^{-1}, being the lowest and highest ones through **TS1′**$_{me,obl}$ and **TS1′**$_{me,per}$, respectively. As a result, the oblique methyl pathway is kinetically favored in the alternative pathway. Even though the nanotube insertion *via* the Magnus mechanism is thermodynamically and kinetically favored as compared to the alternative one, the nanotube coordination is certainly hampered. However, although structures like **CP3**[88,89] and **CP4**[85] had been previously discussed, thus supporting the original idea of Magnus, some **CP3**-like structures were found to hamper the course of the PKR due to an unfavorable relative orientation of the cobalt-coordinated alkyne and alkene.[84] Consequently, we conclude that the Magnus mechanism is only favored in those cases in which **CP3** is more stable than **CP1′**; electronic factors like the double-bond delocalization in SWCNTs and the steric hindrance bring about a destabilization of **CP3** resulting in a non-operative Magnus pathway in PKRs involving SWCNTs. Therefore, a favored or hindered PKR may be predicted by **TS1′** rather than **TS1** in terms of kinetic arguments. Consequently, the PKR at this stage of the reaction should preferably proceed *via* **TS1′**$_{me,obl}$ because of the lowest energy barrier of 22.6 kcal mol^{-1}.

Henceforth, the alternative pathway converges to the Magnus mechanism such that the following steps are identical for both pathways. The CO insertion is an endergonic process which requires an energy from 5 to 18 kcal mol^{-1} to form **CP6** from **CP5**. The energy barriers in these cases range from 13 to 20 kcal mol^{-1}, being the lowest and highest ones *via* **TS2***$_{bu,obl}$ (**TS2***$_{bu,per}$) and **TS2**$_{me,obl}$ (**TS2**$_{me,per}$, **TS2**$_{bu,obl}$), respectively. Based on these results, it can be concluded that the oblique butyl pathway is kinetically favored at this stage of the reaction. **TS2***$_{bu,obl}$ is 6.9 kcal mol^{-1} lower than **TS2**$_{me,obl}$.

This journal is © The Royal Society of Chemistry 2018

Open Access Article. Published on 25 July 2018. Downloaded on 2/11/2026 3:22:22 AM.
This article is licensed under a Creative Commons Attribution 3.0 Unported Licence.

Nevertheless, it should be taken into consideration that in the previous step **TS1′*$_{bu,obl}$** is 5.6 kcal mol^{-1} higher than **TS1′$_{me,obl}$**. Subsequently, the PKR should rather proceed *via* the oblique position, although both methyl and butyl pathways are feasible so far.

The formation of **CP7** from **CP6** is an exergonic process releasing an energy from 15 to 20 kcal mol^{-1}; then the formation of **PD** is strongly thermodynamically favored because more than 36 kcal mol^{-1} are released through the reductive elimination step. The energy barriers for such a step range from 2 to 13 kcal mol^{-1}, being the lowest and highest ones through **TS3$_{me,per}$** and **TS3$_{bu,obl}$**, respectively. With the exception of **TS3$_{bu,obl}$**, the energy barriers through the distinct pathways are nearly identical since the energy differences among them is less than 2 kcal mol^{-1}; therefore, the PKR proceeds indistinctly at this stage of the reaction. The formation of the **PK** adduct occurs releasing *ca.* 70 kcal mol^{-1} in all the cases. Overall, based on Fig. 2, it is concluded that the turnover-frequency determining intermediate (TDI) and transition state (TDTS)[90–93] are respectively **RC** and **TS1′** (**TS2$_{me,obl}$** has almost the same energy as **TS1′$_{me,obl}$** and both could be considered TDTSs in this case). On the other hand, **CP1** is the TDI and **TS1** is the TDTS for all the Magnus pathways with energy barriers ranging from 41 to 66 kcal mol^{-1}. These results suggest that the alternative pathway is certainly more efficient for the PKR, being the oblique methyl pathway the kinetically most favored with an effective energy barrier (the so-called energetic span) of 22.6 kcal mol^{-1} *via* **TS1′$_{me,obl}$**. As a result, this functionalization is indeed viable under laboratory conditions.

The previous analysis is exactly done in the case of the PKR regarding acetylene resulting in no mechanistic differences (see Fig. S1†); therefore, here we only report the most relevant results. That is, the determinant states are **CP1**, **CP2** and **TS1′**; wherein **CP1** is the TDI in any case, yet the TDTS is **CP2** in the Magnus mechanism leading to an energy barrier of 43.9 kcal mol^{-1}. On the other hand, **TS1′** is the TDTS for the alternative pathway with a more effective energy barrier of 29.4 kcal mol^{-1} *via* **TS1′$_{obl}$**. As a matter of fact, our results suggest that the PKR in (5,5)-SWCNT with acetylene could be difficult to proceed in the laboratory in view of that an energy barrier of at least 29.4 kcal mol^{-1}, *via* **TS1′$_{obl}$**, must be overcome.

The PKR in semimetallic SWCNTs. In the case of the PKR in (9,0)-SWCNT with 2-heptyne, the cycloaddition can occur at the parallel and oblique positions with respect to the nanotube axis; then six **PK** adducts can be differentiated analogous to the previous subsection. The nanotube coordination in the Magnus pathway must overcome an energy barrier of 40.6 kcal mol^{-1} in an endergonic process by 24.4 kcal mol^{-1} to form **CP3$_{me}$** (or 26.4 kcal mol^{-1} to form **CP3$_{bu}$**). The nanotube insertion leading to **CP4$_{me,par}$** from **CP3$_{me}$** involves an energy barrier of 23.6 kcal mol^{-1} in an endergonic process by 17.4 kcal mol^{-1}. However, given that **CP1** is the TDI and **TS1$_{me,par}$** is the TDTS in the Magnus mechanism, the overall energy barrier reaches 48.0 kcal mol^{-1} (see Fig. 3). Even though we did not perform calculations for the other five pathways (*i.e. via* **TS1$_{me,obl}$**, **TS1*$_{me,obl}$**, **TS1$_{bu,par}$**, **TS1$_{bu,obl}$**, and **TS1*$_{bu,obl}$**),

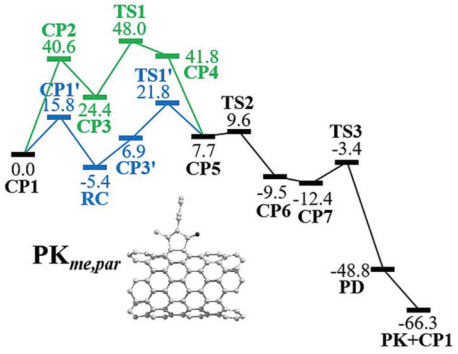

Fig. 3 Gibbs energy profiles in kcal mol^{-1} for the Pauson–Khand reaction with 2-heptyne in (9,0)-SWCNT *via* the parallel methyl pathway. Blue and green lines respectively correspond to the alternative and generally-accepted pathways. The alternative pathway converges to the generally-accepted mechanism (black line).

the current outcomes and the results obtained in the former subsection suggest that the Magnus mechanism is kinetically less favored. In view of that, now we focus on the cycloaddition *via* the alternative pathway to (9,0)-SWCNT with 2-heptyne; indeed, unlike the Magnus mechanism, this pathway is an exergonic process releasing from 5 to 7 kcal mol^{-1} to form **RC** with a lower energy barrier of *ca.* 16 kcal mol^{-1} *via* **CP1′**.

The nanotube insertion *via* the alternative pathway is an endergonic process requiring an energy gain from 13 to 28 kcal mol^{-1} to form **CP5** from **RC**. Energy barriers in this step range from 27 to 46 kcal mol^{-1}, being the lowest and highest ones through **TS1′$_{me,par}$** and **TS1′*$_{bu,obl}$**, respectively (details in Table S1†). As a result, the parallel methyl pathway is kinetically favored in the alternative mechanism. According to Fig. S1† and related discussion, the same result is obtained for the nanotube insertion of acetylene considering all possible reaction pathways. Therefore and because of the size of the systems, henceforth we only describe the parallel pathway which is the most reactive position (see Fig. 3).

The CO insertion is an exergonic process which releases 17.2 and 24.4 kcal mol^{-1}, respectively, to form **CP6$_{me,par}$** and **CP6$_{bu,par}$** from **CP5$_{me,par}$** and **CP5$_{bu,par}$**. The energy barrier in this step is small, *ca.* 2 kcal mol^{-1}. The reductive elimination *via* **TS3$_{me,par}$** occurs with a lower energy barrier (9.0 kcal mol^{-1}) as compared to **TS3$_{bu,par}$** (12.0 kcal mol^{-1}); as a result, the parallel methyl pathway is still kinetically favored. The formation of **PD** and **PK** is given with an energy stabilization of at least 36 kcal mol^{-1}. In general, in both the methyl and butyl pathways, the TDI is **RC** and the TDTS is **TS1′**, being the lowest energy barrier *via* **TS1′$_{me,par}$**, 27.2 kcal mol^{-1}. Then, in view of the effective energy barrier of 22.6 kcal mol^{-1} for the PKR in (5,5)-SWCNT with 2-heptyne, we conclude that the armchair SWCNTs react faster than the semimetallic zig-zag ones.

Finally, in the case of the PKR considering acetylene, the TDTS is **TS1′** in the alternative pathway and the energy barrier of 29.2 kcal mol^{-1} *via* **TS1′$_{par}$** is at least 3.8 kcal mol^{-1} lower than the ones in the oblique pathways; indeed, it is a more

Open Access Article. Published on 25 July 2018. Downloaded on 2/11/2026 3:22:22 AM.
This article is licensed under a Creative Commons Attribution 3.0 Unported Licence.

effective activation energy than that of 43.9 kcal mol^{-1} *via* the Magnus mechanism. Besides, since **PK$_{par}$** is the most stable adduct, it is concluded that the parallel pathway is the most kinetically and thermodynamically favored reaction mechanism. As a final remark, it should be noticed that the energy barrier of 29.2 kcal mol^{-1} *via* **TS1′$_{par}$** in (9,0)-SWCNT is identical to that one *via* **TS1′$_{obl}$** in (5,5)-SWCNT, 29.4 kcal mol^{-1}; therefore, both metallic armchair and semimetallic zig-zag SWCNTs may not be thermally functionalized with acetylene under laboratory conditions.

The PKR in semiconducting SWCNTs. Based on the results from the previous subsections, we study the PKR with 2-heptyne for semiconducting SWCNTs only at the TDTS of the alternative pathway, **TS1′**. The selected models are the 3-Clar unit cells (6,5)- and (8,0)-SWCNT with diameters of 7.47 and 6.26 Å, respectively. The energy barrier *via* **TS1′$_{me,obl}$** for (6,5)-SWCNT and **TS1′$_{me,par}$** for (8,0)-SWCNT is 15.1 kcal mol^{-1} in both cases; the TDTS is **CP1′** since the energy cost for its formation is 15.8 kcal mol^{-1}. These results suggest that the semiconducting SWCNTs react faster than any other ones. Then, given that the diameters of the SWCNTs under study are almost identical, within a range of 1.3 Å, we conclude that electronic factors are more important than the effect of the curvature. However, a reduced reactivity is expected as the diameter increases.[67,94]

Origin of the regioselectivity of the PKR in SWCNTs. Scheme 1 illustrates the dependence of the PKR on either structural conformations or electronic interactions. To explain the regioselectivity of the PKR in SWCNTs, we make use of the activation strain model (ASM),[95–98] also known as the distortion/interaction model.[99–102] The ASM is a helpful tool to better understand the origin of energy barriers. These barriers are analyzed in terms of strain and interaction energies between the fragments participating in the formation or rupture of chemical bonds. In the ASM, activation energies can be separated into strain and interaction energies, *i.e.*, $\Delta E^{\ddagger} = \Delta E^{\ddagger}_{\text{strain}} + \Delta E^{\ddagger}_{\text{int}}$. The strain energy $\Delta E^{\ddagger}_{\text{strain}}$ is the energy required to deform reactants from their equilibrium geometry into the geometry they acquire in the activated complex; and the transition state interaction $\Delta E^{\ddagger}_{\text{int}}$ is the interaction energy between the deformed reactants in the transition state. This model can be extended through all the structures along a reaction coordinate; but here in Table 2 we only focus on all the TDTS structures under study, that is **TS1′**.

The ASM is firstly discussed for **TS1′** with (5,5)-SWCNT. In the case of 2-heptyne, larger differences in $\Delta E^{\ddagger}_{\text{strain}}(f1)$ are observed, yet the oblique pathway results in significantly smaller deformation (*ca.* 12 kcal mol^{-1}) in the nanotube by at least 9 kcal mol^{-1}. **CP1** is distorted with $\Delta E^{\ddagger}_{\text{strain}}(f2)$ ranging from 66 to 69 kcal mol^{-1}, except for **TS1′*$_{bu,obl}$** (64.1 kcal mol^{-1}) and **TS1′$_{me,obl}$** (62.9 kcal mol^{-1}). $\Delta E^{\ddagger}_{\text{int}}$ results in −70 ± 2 kcal mol^{-1} for all the cases with the exceptions of **TS1′*$_{me,obl}$** (−78.8 kcal mol^{-1}) and **TS1′*$_{bu,obl}$** (−80.4 kcal mol^{-1}). Despite $\Delta E^{\ddagger}_{\text{int}}$ for **TS1′*$_{me,obl}$** and **TS1′*$_{bu,obl}$** are the most favored ones, their $\Delta E^{\ddagger}_{\text{strain}}$ are the highest ones; in fact, even though $\Delta E^{\ddagger}_{\text{int}}$ for **TS1′$_{me,obl}$** is not the most favored, $\Delta E^{\ddagger}_{\text{strain}}$ is the lowest one so that it results in the lowest activation energy. These outcomes certainly suggest that strain is the main factor influencing the PKR in (5,5)-SWCNT.

Table 2 The activation strain model at the TDTS of the PKR with 2-heptyne in (5,5)-SWCNT (upper half) and (9,0)-SWCNT (bottom). The fragment *f*1 stands for the nanotube and *f*2 for the **CP1** fragment. Electronic energies in kcal mol^{-1}

Structure	$\Delta E^{\ddagger}_{\text{str}}$ (*f*1)	$\Delta E^{\ddagger}_{\text{str}}$ (*f*2)	$\Delta E^{\ddagger}_{\text{str}}$	$\Delta E^{\ddagger}_{\text{int}}$	$\Delta E^{\ddagger}$
TS1′$_{me,obl}$	12.6	62.9	75.5	−71.1	4.4
TS1′*$_{me,obl}$	26.0	67.2	93.2	−78.8	14.4
TS1′$_{me,per}$	21.5	67.2	88.7	−68.2	20.5
TS1′$_{bu,obl}$	12.2	68.6	80.8	−70.4	10.4
TS1′*$_{bu,obl}$	26.6	64.1	90.7	−80.4	10.3
TS1′$_{bu,per}$	23.0	66.2	89.2	−71.7	17.5
TS1′$_{me,par}$	24.8	63.2	88.0	−82.4	5.6
TS1′$_{me,obl}$	11.5	63.2	74.7	−60.4	14.3
TS1′*$_{me,obl}$	12.0	70.2	82.2	−64.2	18.0
TS1′$_{bu,par}$	26.0	65.0	91.0	−84.6	6.4
TS1′$_{bu,obl}$	11.2	76.9	88.1	−68.8	19.3
TS1′*$_{bu,obl}$	14.3	70.8	85.1	−60.7	24.4

In the case of the PKR in (9,0)-SWCNT with 2-heptyne, $\Delta E^{\ddagger}_{\text{strain}}(f1)$ in the parallel cycloaddition is higher with a value of *ca.* 25 kcal mol^{-1}, $\Delta E^{\ddagger}_{\text{strain}}(f1)$ is in the range from 11 to 15 kcal mol^{-1}. On the other hand, $\Delta E^{\ddagger}_{\text{strain}}(f2)$ in the parallel cycloaddition is among the lowest ones (63.2 and 65.0 kcal mol^{-1} for the methyl and butyl pathways, respectively). The total $\Delta E^{\ddagger}_{\text{strain}}$ in the parallel cycloadditions are the highest ones (above 88 kcal mol^{-1}), but both pathways also result in the lowest $\Delta E^{\ddagger}_{\text{int}}$ (−82.4 and −84.6 kcal mol^{-1} for the methyl and butyl pathways, respectively) and the lowest activation energies. As a result, it is concluded that the interaction energy is the main factor controlling the course of the PKR in (9,0)-SWCNT. In fact, results in Table S2† and related discussion exactly lead to the same conclusions regarding acetylene for both types of SWCNTs. Moreover, in the case of the PKR in (9,0)-SWCNT with acetylene, an analysis of HOMO–LUMO energies and an energy decomposition analysis, both related to **TS1′** (see Tables S3 and S4†), suggest that the orbital interaction term (better $\text{HOMO}_{\text{nanotube}}$–$\text{LUMO}_{\textbf{CP1}}$ interaction at the TDTS) is the main factor explaining the more stabilizing interaction energy for the parallel attack.

Experimental investigations

To confirm the theoretical predictions, we performed the PKR between three alkynes: 2-heptyne (**1a**), 1-octyne (**1b**), 5-methyl-1-hexyne (**1c**), $Co_2(CO)_8$ and two types of CNTs: HiPco SWCNTs (mixture of metallic and semiconducting SWCNTs in a 1 : 2 ratio, approximately) and (6,5) enriched SWCNTs (with a 95% content of semiconducting tubes) (Scheme 4).

Using HiPco tubes, no reaction was observed for alkyne **1a** in *N*-methyl-2-pyrrolidone (NMP) at 70° C/72 h, neither at 110° C/24 h. Nevertheless, when the reaction was carried out at 110 °C during 72 h, the comparison of Raman spectra of pristine and PK-functionalized SWCNTs (*vide infra*) shows clear evidences of functionalization in the wall of carbon nanotubes.

 This journal is © The Royal Society of Chemistry 2018

Open Access Article. Published on 25 July 2018. Downloaded on 2/11/2026 3:22:22 AM.
This article is licensed under a Creative Commons Attribution 3.0 Unported Licence.

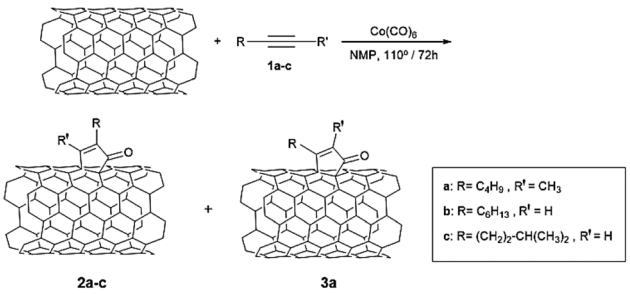

Scheme 4 Chemical modification of SWCNTs under Pauson–Khand reaction.

These reaction conditions were later used in all reactions with both, HiPco tubes and (6,5) enriched SWCNTs.

Thermogravimetric analysis (TGA) was used to confirm the functionalization of CNT samples by comparing the thermogravimetric profiles of the pristine and functionalized materials under inert atmosphere (Fig. S2†). PK-functionalized SWCNTs show an increase of the weight loss with respect to pristine SWCNT. The weight lost is lower for the hybrids formed from the less reactive alkyne **1a**. This confirms the covalent reaction and support the higher reactivity of terminal alkynes; the absence of significant reaction of (6,5) SWCNT and alkyne **1a** (Fig. S2b†) must be remarked.

Raman spectroscopy clearly shows the degree of functionalization of HiPco and (6,5) enriched SWCNTs with the three alkynes **1a–c** (Fig. 4). Firstly, for HiPco SWCNTs (Fig. 4, top), the low defect-related D-band to tangential G-band intensity ratio changes from 0.048 to 0.083 for **2a**, 0.16 for **2b** and 0.12 for **2c** after functionalization; in case of (6,5) enriched SWCNT (Fig. 4, down) similar degree of functionalization changes was observed except for alkyne **1a** confirming the observed by TGA (see above). The increase of D/G ratio confirms the increase of defects after PKR and the success of the reaction. Again, it is remarkable how the degree of functionalization is higher for terminal alkynes **1b** and **1c** rather than central alkyne **1a**. It should be mentioned here that, after the PKR, the G-band of the functionalized carbon nanotubes is shifted to higher frequencies (3–6 cm^{-1}) in comparison with that of pristine SWCNTs (Fig. S3†), thus confirming the p-type doping of carbon nanotubes as consequence of the attached carbonyl moiety.[103] The higher shift is visible for the more functionalization materials. This shift can be also observed in the 2D band (Fig. S4†).[104] Moreover, analysis of the RBM zone (Fig. S5†) shows, for pristine HiPco SWCNT, two contributions, one at 231 cm^{-1} and the other at 265 cm^{-1} corresponding to a tube diameter of 1.03 nm and 0.89 nm respectively.[105] After PKR, the band ascribed to lower diameter reduces its intensity as a consequence of the high reactivity of smaller tubes. Same behaviour is observed for enriched (6,5) SWCNT, reduction of the lowest diameter tube (0.89 nm).

Information derived from X-ray photoelectron spectroscopy is in agreement with Raman spectroscopy data. In XPS, comparison of the high-resolution C 1s spectra (Fig. S6–S9†) of

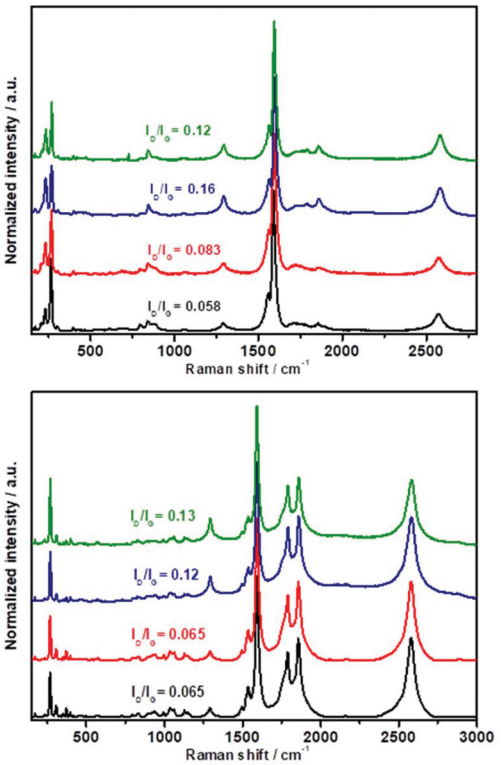

Fig. 4 Raman spectra (excitation wavelength 785 nm) of pristine HipCo (top) and (6,5) SWCNTs (—) (bottom) and PK-functionalized HiPco (top) and (6,5) (bottom) enriched SWCNTs with alkyne **1a** (—), **1b** (—), and **1c** (—). Intensities have been normalized to the G-band (highest peak).

pristine SWCNTs and PK-functionalized SWCNTs (HiPco and (6,5)) confirms the sidewall covalent functionalization due to appearance of new carbon component at 285.9 eV corresponding to sp^3 C atoms,[104] which is visible in all CNT hybrids.

Covalent functionalization is known to quench carbon nanotubes photoluminescence;[105] so, the emission features of PK-functionalized SWCNTs were compared with those of pristine SWCNTs, both dispersed in sodium dodecylbenzene sulfonate (SDBS). Photoluminescence maps of pristine enriched (6,5) SWCNT and PK-functionalized SWCNT with **1b** and **1c** are shown in Fig. 5 and Fig. S10† respectively; red shift of 4–8 nm for (6,5) peak are observed after PK reaction, ascribed to the electron-withdrawing effect of the cyclopentenone ring. Also, new component at 1117 nm corresponded to E_{11}^- formation. These results confirmed the (6,5) SWCNTs reactivity and the formation of defects on the sidewall of CNTs.

On the other hand, (Fig. S11†), from photoluminescence spectra for functionalized HiPco SWCNT with respect to pristine HiPco tubes, a remarkable intensity variation is evident despite not being homogeneous for all chiralities. Upon a more detailed inspection for the hybrids derived from reaction with **1a**, red shifts of peak position are observed for PK-functionalized HiPco SWCNTs (Fig. S11†). In particular, the (10,2) and (8,4) are shifted from 1055 nm to 1062 nm and from 1113 nm to 1118 nm, respectively. Nevertheless, shift of only

Open Access Article. Published on 25 July 2018. Downloaded on 2/11/2026 3:22:22 AM.
This article is licensed under a Creative Commons Attribution 3.0 Unported Licence.

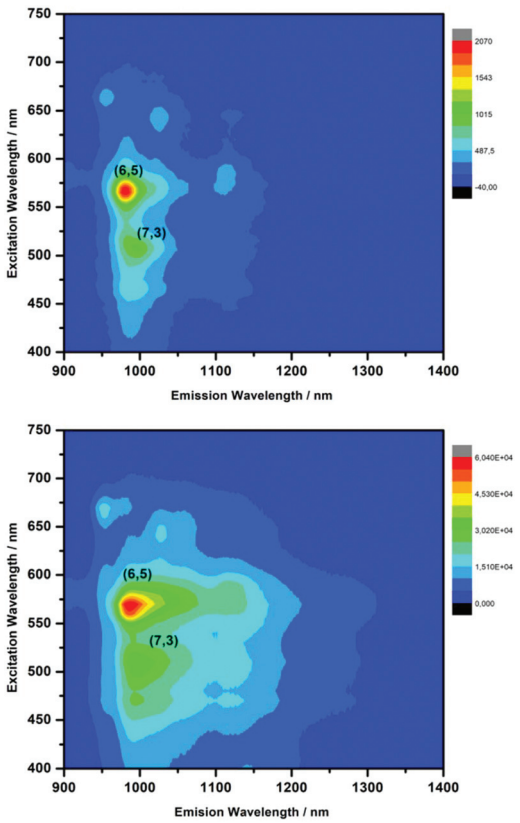

Fig. 5 3D-photoluminescence plot of: (top) pristine (6,5) enriched SWCNTs and (bottom) PK-functionalized (6,5) enriched SWCNTs with **1b** in D_2O at room temperature.

0–1 nm is observed for (9,4) and (7,6) peaks. Similar shifts are observed for reaction with **1b** and **1c**. As a final remark, the results obtained by the experimental investigation corroborate the theoretical predictions: SWCNTs can be indeed chemically functionalized *via* the PKR with accessible energy barriers for the semiconducting and metallic types.

Conclusions

We theoretically and experimentally studied the Pauson–Khand reaction (PKR) catalyzed by $Co_2(CO)_8$ between carbon monoxide, several alkynes, and three types of single-walled carbon nanotubes (SWCNTs). Accurate and broad quantum chemical exploration of this [2 + 2 + 1] cycloaddition provided evidence for an alternative reaction mechanism operative in SWCNTs that appears to be more viable than the traditional mechanism proposed by Magnus. In the mechanism that we established, the turnover-frequency determining transition state (TDTS) of the PKR is given by the nanotube-insertion step, **TS1′**. For metallic and semimetallic SWCNTs reacting with acetylene, the associated Gibbs activation energy of 29 kcal mol^{-1} is too high to be viable under laboratory conditions. On the other hand, the effective Gibbs energy barrier in the PKR with 2-heptyne amounts to 27.2 kcal mol^{-1} for the semimetallic (9,0)-SWCNT, 22.6 kcal mol^{-1} for the metallic (5,5)-SWCNT, and only 15.8 kcal mol^{-1} for the semiconducting (6,5)- and (8,0)-SWCNT. These results suggest that semiconducting SWCNTs react faster than any other, although metallic ones are also prone to PK-functionalization because of the accessible energy barrier of 22.6 kcal mol^{-1}. Moreover, the cycloaddition is regioselective as it takes place exclusively at the oblique position of armchair SWCNTs and at the parallel position of zig-zag SWCNTs.

Finally, guided by our theoretical predictions, we were able to generate PK adducts of SWCNTs using one central and two terminal alkynes in the laboratory under simple heating. Both mixtures of metallic/semiconducting and enriched semiconducting SWCNTs were PK-functionalized in agreement with the theoretical results. The characterization based on Raman spectroscopy supported by XPS, TGA, and photoluminescence analyses confirmed the successful synthesis of PK adducts. Terminal alkynes showed a higher reactivity. In addition, the PKR did not proceed with alkynes of lower molecular weight, which is in accordance with the higher DFT energy barriers predicted for the PKR with acetylene. We envisage that our proposed mechanism for the PKR may help develop synthetic routes more efficiently.

Experimental details

A suspension of pristine HiPco SWCNTs or enriched (6,5) SWCNT (10 mg) in *N*-methyl-2-pyrrolidone (NMP) (25 mL) was sonicated for 15 minutes and then the alkyne (0.83 mmol) was added. On the other hand, a suspension of $Co_2(CO)_8$ (0.083 mmol) in NMP (25 mL) was sonicated for 15 minutes and then added to the suspension of pristine SWCNTs and alkyne **1a–c**. The reaction mixture was stirred at 110 °C for 72 hours under inert atmosphere. After cooling to room temperature, the suspension was filtered with a PTFE membrane and the solid was washed successively with NMP and CH_2Cl_2. The black solid was dispersed in 3 mL of water/SDBS 5 wt%. The solution was first sonicated in bath sonicator for 30 minutes; next, the obtained solution was sonicated for 1 min using a tip sonicator. The PK-functionalized SWCNTs were exfoliated after these treatment, and the undissolved particles that correspond to the unreacted $Co_2(CO)_8$ were settle after centrifuged for 1 min under 3000 rpm. The obtained dark solution was then centrifuged at 14 000 rpm to deposit the PK-functionalized SWCNT. The black solid was washed subsequently with water and acetone to remove the excess of SDBS.

Computational details

All calculations were done with the Amsterdam Density Functional (ADF, 2013) program at the BP86-D_3BJ level of theory.[106–116] Molecular orbitals were expanded in uncontracted sets of Slater-type orbitals (STOs) of double-ζ (DZP: for H, C, O atoms) and triple-ζ quality (TZP: for Co) containing one set of polarization and diffuse functions. The frozen-core approximation (FCA) was employed for the 1s core of carbon and oxygen atoms, and the 1s2s2p core of Co.[106] The FCA has

 This journal is © The Royal Society of Chemistry 2018

Open Access Article. Published on 25 July 2018. Downloaded on 2/11/2026 3:22:22 AM.
This article is licensed under a Creative Commons Attribution 3.0 Unported Licence.

been shown to have a negligible effect on the geometry optimization procedure.[117,118] In addition, scalar relativistic corrections were added within the zeroth-order regular approximation (ZORA).[119]

All geometry optimizations were performed by the quantum regions interconnected by local descriptions (QUILD) code.[120] This latter works as a wrapper around the ADF program since it creates input files for ADF, then executes this program and collects energies and gradients. QUILD uses adapted delocalized coordinates and constructs model Hessians with the appropriate number of eigenvalues; which results in an advantage in the determination of transition state structures.[121] All the stationary points were analyzed through analytical vibrational frequencies as calculated at the BP86(D_3-BJ)/DZP (TZP: for cobalt) including FCA and ZORA. Low frequencies were recalculated *via* the *scanfreq* keyword[106] since frequencies that have a small force constant are more sensitive to the numerical noise. For a more detailed description of the determination of stationary points, see the ESI.†

Electronic energies were corrected in a single-point approach at the O3LYP[122,123](D_3-BJ)/TZP//BP86(D_3-BJ)/DZP (TZP: for cobalt) level of theory including FCA and ZORA. Solvent effects due to *N*-methyl-2-pyrrolidone (with a dielectric constant of 33.0) were incorporated *via* the conductor-like screening model (COSMO)[124] as implemented in ADF. Gibbs energies were determined from the corrected electronic energies. Furthermore, corrections of the zero-point energy, thermal contributions to the internal energy, and the entropy term were computed from vibrational frequencies at 298.15 K considering an ideal gas in standard conditions. In a performance test of various functionals, we have verified that our O3LYP-corrected approach reproduces best the activation Gibbs energy obtained from kinetic studies based on ^{1}H nuclear magnetic resonance spectroscopy (complete details in Fig. S12 and Table S5†).[125]

Conflicts of interest

The authors declare no competing financial interest.

Acknowledgements

Excellent service by the Stichting Academisch Rekencentrum Amsterdam (SARA) and the Consorci de Serveis Universitaris de Catalunya (CSUC) is gratefully acknowledged. A. P. and F. L. thank the Spanish MINECO for projects CTQ2014-59832-JIN and CTQ2016-79189-R, respectively. M. S. thanks EU for a FEDER fund (UNGI08-4E-003), the Generalitat de Catalunya for project 2017SGR39, the Xarxa de Referència en Química Teòrica I Computacional, and ICREA Academia 2014 prize, and MINECO of Spain through project CTQ2017-85341-P. M. V. thanks CYTEMA-SANTANDER for a postdoctoral grant and L. M. A. thanks the Spanish MINECO for a FPI grant.

Notes and references

1 I. U. Khand, G. R. Knox, P. L. Pauson and W. E. Watts, *J. Chem. Soc. D*, 1971, 36a–36a.
2 I. U. Khand, G. R. Knox, P. L. Pauson and W. E. Watts, *J. Chem. Soc., Perkin Trans. 1*, 1973, 975–977.
3 I. U. Khand, G. R. Knox, P. L. Pauson, W. E. Watts and M. I. Foreman, *J. Chem. Soc., Perkin Trans. 1*, 1973, 977–981.
4 C. Exon and P. Magnus, *J. Am. Chem. Soc.*, 1983, **105**, 2477–2478.
5 P. Magnus, L. M. Principe and M. J. Slater, *J. Org. Chem.*, 1987, **52**, 1483–1486.
6 N. E. Schore and E. G. Rowley, *J. Am. Chem. Soc.*, 1988, **110**, 5224–5225.
7 M. E. Price and N. E. Schore, *J. Org. Chem.*, 1989, **54**, 5662–5667.
8 J. Castro, H. Sorensen, A. Riera, C. Morin, A. Moyano, M. A. Pericas and A. E. Greene, *J. Am. Chem. Soc.*, 1990, **112**, 9388–9389.
9 I. Nomura and C. Mukai, *J. Org. Chem.*, 2004, **69**, 1803–1812.
10 T. Kozaka, N. Miyakoshi and C. Mukai, *J. Org. Chem.*, 2007, **72**, 10147–10154.
11 Y. Hayashi, F. Inagaki and C. Mukai, *Org. Lett.*, 2011, **13**, 1778–1780.
12 K. Fujioka, H. Yokoe, M. Yoshida and K. Shishido, *Org. Lett.*, 2012, **14**, 244–247.
13 J. Blanco-Urgoiti, L. Añorbe, L. Pérez-Serrano, G. Domínguez and J. Pérez-Castells, *Chem. Soc. Rev.*, 2004, **33**, 32–42.
14 H.-W. Lee and F.-Y. Kwong, *Eur. J. Org. Chem.*, 2010, 789–811.
15 J. Solà, A. Riera, X. Verdaguer and M. A. Maestro, *J. Am. Chem. Soc.*, 2005, **127**, 13629–13633.
16 M. Revés, T. Achard, J. Solà, A. Riera and X. Verdaguer, *J. Org. Chem.*, 2008, **73**, 7080–7087.
17 S. Kitagaki, F. Inagaki and C. Mukai, *Chem. Soc. Rev.*, 2014, **43**, 2956–2978.
18 S. P. Simeonov, J. P. M. Nunes, K. Guerra, V. B. Kurteva and C. A. M. Afonso, *Chem. Rev.*, 2016, **116**, 5744–5893.
19 N. Jeong, S. Lee and B. K. Sung, *Organometallics*, 1998, **17**, 3642–3644.
20 K. H. Park, S. U. Son and Y. K. Chung, *Tetrahedron Lett.*, 2003, **44**, 2827–2830.
21 D. E. Kim, I. S. Kim, V. Ratovelomanana-Vidal, J.-P. Genêt and N. Jeong, *J. Org. Chem.*, 2008, **73**, 7985–7989.
22 T. Morimoto, N. Chatani, Y. Fukumoto and S. Murai, *J. Org. Chem.*, 1997, **62**, 3762–3765.
23 T. Kondo, N. Suzuki, T. Okada and T. Mitsudo, *J. Am. Chem. Soc.*, 1997, **119**, 6187–6188.
24 L.-J. Deng, J. Liu, J.-Q. Huang, Y. Hu, M. Chen, Y. Lan, J.-H. Chen, A. Lei and Z. Yang, *Synthesis*, 2007, 2565–2570.
25 T. Shibata and K. Takagi, *J. Am. Chem. Soc.*, 2000, **122**, 9852–9853.
26 T. Shibata, N. Toshida, M. Yamasaki, S. Maekawa and K. Takagi, *Tetrahedron*, 2005, **61**, 9974–9979.

Open Access Article. Published on 25 July 2018. Downloaded on 2/11/2026 3:22:22 AM.
This article is licensed under a Creative Commons Attribution 3.0 Unported Licence.

27 A. J. Pearson and R. A. Dubbert, *J. Chem. Soc., Chem. Commun.*, 1991, 202–203.
28 A. J. Pearson and R. A. Dubbert, *Organometallics*, 1994, **13**, 1656–1661.
29 T. R. Hoye and J. A. Suriano, *J. Am. Chem. Soc.*, 1993, **115**, 1154–1156.
30 C. Mukai, M. Uchiyama and M. Hanaoka, *J. Chem. Soc., Chem. Commun.*, 1992, 1014–1015.
31 N. Jeong, S. J. Lee, B. Y. Lee and Y. K. Chung, *Tetrahedron Lett.*, 1993, **34**, 4027–4030.
32 T. R. Hoye and J. A. Suriano, *Organometallics*, 1992, **11**, 2044–2050.
33 L. Jordi, A. Segundo, F. Camps, S. Ricart and J. M. Moreto, *Organometallics*, 1993, **12**, 3795–3797.
34 F. Robert, A. Milet, Y. Gimbert, D. Konya and A. E. Greene, *J. Am. Chem. Soc.*, 2001, **123**, 5396–5400.
35 T. J. M. de Bruin, C. Michel, K. Vekey, A. E. Greene, Y. Gimbert and A. Milet, *J. Organomet. Chem.*, 2006, **691**, 4281–4288.
36 E. Fager-Jokela, M. Muuronen, M. Patzschke and J. Helaja, *J. Org. Chem.*, 2012, **77**, 9134–9147.
37 E. Fager-Jokela, M. Muuronen, H. Khaizourane, A. Vázquez-Romero, X. Verdaguer, A. Riera and J. Helaja, *J. Org. Chem.*, 2014, **79**, 10999–11010.
38 R. R. Torres, *The Pauson–Khand Reaction: Scope, Variations and Applications*, John Wiley & Sons, 2012.
39 N. Martín, M. Altable, S. Filippone and A. Martín-Domenech, *Chem. Commun.*, 2004, 1338–1339.
40 N. Martín, M. Altable, S. Filippone, A. Martín-Domenech, A. Poater and M. Solà, *Chem. – Eur. J.*, 2005, **11**, 2716–2729.
41 S. Su, R. A. Rodriguez and P. S. Baran, *J. Am. Chem. Soc.*, 2011, **133**, 13922–13925.
42 N. Aiguabella, A. Pesquer, X. Verdaguer and A. Riera, *Org. Lett.*, 2013, **15**, 2696–2699.
43 A. Vázquez-Romero, L. Cárdenas, E. Blasi, X. Verdaguer and A. Riera, *Org. Lett.*, 2009, **11**, 3104–3107.
44 A. Vázquez-Romero, J. Rodríguez, A. Lledó, X. Verdaguer and A. Riera, *Org. Lett.*, 2008, **10**, 4509–4512.
45 A. Cabré, X. Verdaguer and A. Riera, *Synthesis*, 2017, **49**, 3945–3951.
46 A. Cabré, H. Khaizourane, M. Garçon, X. Verdaguer and A. Riera, *Org. Lett.*, 2018, **20**, 3953–3957.
47 Y. H. Yang and W. Z. Li, *Appl. Phys. Lett.*, 2011, **98**, 041901.
48 M. M. J. Treacy, T. W. Ebbesen and J. M. Gibson, *Nature*, 1996, **381**, 678–680.
49 E. Thostenson, C. Li and T. Chou, *Compos. Sci. Technol.*, 2005, **65**, 491–516.
50 E. Pop, D. Mann, Q. Wang, K. Goodson and H. Dai, *Nano Lett.*, 2006, **6**, 96–100.
51 M. Ouyang, J.-L. Huang and C. M. Lieber, *Acc. Chem. Res.*, 2002, **35**, 1018–1025.
52 M. E. Itkis, S. Niyogi, M. E. Meng, M. A. Hamon, H. Hu and R. C. Haddon, *Nano Lett.*, 2002, **2**, 155–159.
53 H. Kataura, Y. Kumazawa, Y. Maniwa, I. Umezu, S. Suzuki, Y. Ohtsuka and Y. Achiba, *Synth. Met.*, 1999, **103**, 2555–2558.
54 C. A. Dyke and J. M. Tour, *J. Phys. Chem. A*, 2004, **108**, 11151–11159.
55 Y.-P. Sun, K. Fu, Y. Lin and W. Huang, *Acc. Chem. Res.*, 2002, **35**, 1096–1104.
56 M. Prato, K. Kostarelos and A. Bianco, *Acc. Chem. Res.*, 2008, **41**, 60–68.
57 J. G. Duque, A. N. G. Parra-Vasquez, N. Behabtu, M. J. Green, A. L. Higginbotham, B. K. Price, A. D. Leonard, H. K. Schmidt, B. Lounis, J. M. Tour, S. K. Doorn, L. Cognet and M. Pasquali, *ACS Nano*, 2010, **4**, 3063–3072.
58 A. Criado, M. J. Gómez-Escalonilla, J. L. G. Fierro, A. Urbina, D. Peña, E. Guitián and F. Langa, *Chem. Commun.*, 2010, **46**, 7028–7030.
59 D. Tasis, N. Tagmatarchis, A. Bianco and M. Prato, *Chem. Rev.*, 2006, **106**, 1105–1136.
60 T. Yang, X. Zhao and S. Nagase, *J. Comput. Chem.*, 2013, **34**, 2223–2232.
61 A. Criado, M. Vizuete, M. J. Gómez-Escalonilla, S. García-Rodriguez, J. L. G. Fierro, A. Cobas, D. Peña, E. Guitián and F. Langa, *Carbon*, 2013, **63**, 140–148.
62 V. O. Koroteev, L. G. Bulusheva, I. P. Asanov, E. V. Shlyakhova, D. V. Vyalikh and A. V. Okotrub, *J. Phys. Chem. C*, 2011, **115**, 21199–21204.
63 P. Magnus, C. Exon and P. Albaugh-Robertson, *Tetrahedron*, 1985, **41**, 5861–5869.
64 P. Magnus and L. M. Principe, *Tetrahedron Lett.*, 1985, **26**, 4851–4854.
65 M. Yamanaka and E. Nakamura, *J. Am. Chem. Soc.*, 2001, **123**, 1703–1708.
66 M. A. Pericàs, J. Balsells, J. Castro, I. Marchueta, A. Moyano, A. Riera, J. Vázquez and X. Verdaguer, *Pure Appl. Chem.*, 2002, **74**, 167–174.
67 J. P. Martínez, F. Langa, F. M. Bickelhaupt, S. Osuna and M. Solà, *J. Phys. Chem. C*, 2016, **120**, 1716–1726.
68 Y. Matsuo, K. Tahara and E. Nakamura, *Org. Lett.*, 2003, **5**, 3181–3184.
69 M. Baldoni, A. Sgamellotti and F. Mercuri, *Org. Lett.*, 2007, **9**, 4267–4270.
70 M. Baldoni, D. Selli, A. Sgamellotti and F. Mercuri, *J. Phys. Chem. C*, 2009, **113**, 862–866.
71 E. Clar, *The Aromatic Sextet*, Wiley, New York, 1972.
72 M. Solà, *Front. Chem.*, 2013, **1**, 22.
73 S. Osuna, M. Torrent-Sucarrat, M. Solà, P. Geerlings, C. P. Ewels and G. Van Lier, *J. Phys. Chem. C*, 2010, **114**, 3340–3345.
74 F. J. Martín-Martínez, S. Melchor and J. A. Dobado, *Phys. Chem. Chem. Phys.*, 2011, **13**, 12844–12857.
75 M. Garcia-Borràs, S. Osuna, J. M. Luis, M. Swart and M. Solà, *Chem. Soc. Rev.*, 2014, **43**, 5089–5105.
76 F. J. Martín-Martínez, S. Melchor and J. A. Dobado, *Org. Lett.*, 2008, **10**, 1991–1994.
77 J. Zhao and P. B. Balbuena, *J. Phys. Chem. C*, 2008, **112**, 3482–3488.
78 T. Pankewitz and W. Klopper, *J. Phys. Chem. C*, 2007, **111**, 18917–18926.

This journal is © The Royal Society of Chemistry 2018

Open Access Article. Published on 25 July 2018. Downloaded on 2/11/2026 3:22:22 AM.
This article is licensed under a Creative Commons Attribution 3.0 Unported Licence.

79 F. Baert, A. Guelzim, J. M. Poblet, R. Wiest, J. Demuynck and M. Benard, *Inorg. Chem.*, 1986, **25**, 1830–1841.
80 C. M. Gordon, M. Kiszka, I. R. Dunkin, W. J. Kerr, J. S. Scott and J. Gebicki, *J. Organomet. Chem.*, 1998, **554**, 147–154.
81 S. M. Draper, C. Long and B. M. Myers, *J. Organomet. Chem.*, 1999, **588**, 195–199.
82 M. E. Krafft, I. L. Scott, R. H. Romero, S. Feibelmann and C. E. Van Pelt, *J. Am. Chem. Soc.*, 1993, **115**, 7199–7207.
83 X. Verdaguer, A. Moyano, M. A. Pericas, A. Riera, V. Bernardes, A. E. Greene, A. Alvarez-Larena and J. F. Piniella, *J. Am. Chem. Soc.*, 1994, **116**, 2153–2154.
84 S. A. Brusey, E. V. Banide, S. Dörrich, P. O'Donohue, Y. Ortin, H. Müller-Bunz, C. Long, P. Evans and M. J. McGlinchey, *Organometallics*, 2009, **28**, 6308–6319.
85 M. K. Pallerla, G. P. A. Yap and J. M. Fox, *J. Org. Chem.*, 2008, **73**, 6137–6141.
86 A. D. Becke, *J. Chem. Phys.*, 1993, **98**, 5648–5652.
87 C. Lee, W. Yang and R. G. Parr, *Phys. Rev. B: Condens. Matter Mater. Phys.*, 1988, **37**, 785–789.
88 Y. Gimbert, D. Lesage, A. Milet, F. Fournier, A. E. Greene and J.-C. Tabet, *Org. Lett.*, 2003, **5**, 4073–4075.
89 E. V. Banide, H. Müller-Bunz, A. R. Manning, P. Evans and M. J. McGlinchey, *Angew. Chem., Int. Ed.*, 2007, **46**, 2907–2910.
90 S. Kozuch and S. Shaik, *J. Phys. Chem. A*, 2008, **112**, 6032–6041.
91 A. Uhe, S. Kozuch and S. Shaik, *J. Comput. Chem.*, 2011, **32**, 978–985.
92 S. Kozuch and J. M. L. Martin, *ChemPhysChem*, 2011, **12**, 1413–1418.
93 S. Kozuch and S. Shaik, *Acc. Chem. Res.*, 2011, **44**, 101–110.
94 J. Li, G. Jia, Y. Zhang and Y. Chen, *Chem. Mater.*, 2006, **18**, 3579–3584.
95 W.-J. van Zeist and F. M. Bickelhaupt, *Org. Biomol. Chem.*, 2010, **8**, 3118–3127.
96 F. M. Bickelhaupt, *J. Comput. Chem.*, 1999, **20**, 114–128.
97 I. Fernández and F. M. Bickelhaupt, *Chem. Soc. Rev.*, 2014, **43**, 4953–4967.
98 L. P. Wolters and F. M. Bickelhaupt, *Wiley Interdiscip. Rev.: Comput. Mol. Sci.*, 2015, **5**, 324–343.
99 K. N. Houk, R. W. Gandour, R. W. Strozier, N. G. Rondan and L. A. Paquette, *J. Am. Chem. Soc.*, 1979, **101**, 6797–6802.
100 D. H. Ess and K. N. Houk, *J. Am. Chem. Soc.*, 2007, **129**, 10646–10647.
101 Y. Cao, Y. Liang, L. Zhang, S. Osuna, A.-L. M. Hoyt, A. L. Briseno and K. N. Houk, *J. Am. Chem. Soc.*, 2014, **136**, 10743–10751.
102 F. M. Bickelhaupt and K. N. Houk, *Angew. Chem., Int. Ed.*, 2017, **56**, 10070–10086.
103 A. Jorio, A. G. Souza Filho, G. Dresselhaus, M. S. Dresselhaus, A. K. Swan, M. S. Ünlü, B. B. Goldberg, M. A. Pimenta, J. H. Hafner, C. M. Lieber and R. Saito, *Phys. Rev. B: Condens. Matter Mater. Phys.*, 2002, **65**, 155412.
104 T. I. T. Okpalugo, P. Papakonstantinou, H. Murphy, J. McLaughlin and N. M. D. Brown, *Carbon*, 2005, **43**, 153–161.
105 M. S. Strano, C. A. Dyke, M. L. Usrey, P. W. Barone, M. J. Allen, H. Shan, C. Kittrell, R. H. Hauge and R. E. Smalley, *Science*, 2003, **301**, 1519–1522.
106 G. te Velde, F. M. Bickelhaupt, E. J. Baerends, C. Fonseca Guerra, S. J. A. van Gisbergen, J. G. Snijders and T. Ziegler, *J. Comput. Chem.*, 2001, **22**, 931–967.
107 S. J. A. van Gisbergen, J. G. Snijders and E. J. Baerends, *Comput. Phys. Commun.*, 1999, **118**, 119–138.
108 C. Fonseca Guerra, J. G. Snijders, G. te Velde and E. J. Baerends, *Theor. Chem. Acc.*, 1998, **99**, 391–403.
109 A. D. Becke, *Phys. Rev. A*, 1988, **38**, 3098–3100.
110 J. Perdew, *Phys. Rev. B: Condens. Matter Mater. Phys.*, 1986, **33**, 8822–8824.
111 S. Grimme, J. Antony, S. Ehrlich and H. Krieg, *J. Chem. Phys.*, 2010, **132**, 154104.
112 S. Grimme, S. Ehrlich and L. Goerigk, *J. Comput. Chem.*, 2011, **32**, 1456–1465.
113 S. Grimme, *Wiley Interdiscip. Rev.: Comput. Mol. Sci.*, 2011, **1**, 211–228.
114 S. Osuna, M. Swart and M. Solà, *J. Phys. Chem. A*, 2011, **115**, 3491–3496.
115 J. P. Martínez, D. E. Trujillo-González, A. W. Götz, F. L. Castillo-Alvarado and J. I. Rodríguez, *J. Phys. Chem. C*, 2017, **121**, 20134–20140.
116 J. P. Martínez, E. Rivera-Avalos, S. Vega-Rodríguez and D. de Loera, *Res. Chem. Intermed.*, 2018, **44**, 2061–2073.
117 J. G. Snijders and M. Swart, *Theor. Chem. Acc.*, 2003, **110**, 34–41.
118 M. Swart and J. G. Snijders, *Theor. Chem. Acc.*, 2004, **111**, 56–56.
119 E. van Lenthe, E. J. Baerends and J. G. Snijders, *J. Chem. Phys.*, 1993, **99**, 4597.
120 M. Swart and F. M. Bickelhaupt, *J. Comput. Chem.*, 2008, **29**, 724–734.
121 M. Swart and F. M. Bickelhaupt, *Int. J. Quantum Chem.*, 2006, **106**, 2536–2544.
122 N. C. Handy and A. J. Cohen, *Mol. Phys.*, 2001, **99**, 403–412.
123 W.-M. Hoe, A. J. Cohen and N. C. Handy, *Chem. Phys. Lett.*, 2001, **341**, 319–328.
124 A. Klamt, *J. Phys. Chem.*, 1995, **99**, 2224–2235.
125 D. R. Hartline, M. Zeller and C. Uyeda, *Angew. Chem., Int. Ed.*, 2016, **55**, 6084–6087.